

See discussions, stats, and author profiles for this publication at: <https://www.researchgate.net/publication/340258585>

A geologic model for lunar ice deposits at mining scales

Article in *Icarus* · March 2020

DOI: 10.1016/j.icarus.2020.113778

CITATIONS

0

READS

194

2 authors, including:

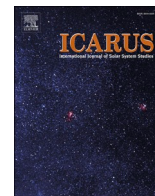


Kevin Cannon

University of Central Florida

23 PUBLICATIONS 152 CITATIONS

SEE PROFILE



Research Paper

A geologic model for lunar ice deposits at mining scales

Kevin M. Cannon^{*}, Daniel T. Britt

University of Central Florida, Department of Physics, 4111 Libra Drive, Physical Sciences Building 430, Orlando, FL 32816, United States of America

ARTICLE INFO

Keywords:
Moon
Ices
Regoliths

ABSTRACT

Water ice has been detected at the lunar poles, but existing and near-future orbital datasets do not have the capabilities to determine its horizontal and vertical distribution at meter to hundred-meter scales relevant for mining operations. Additionally, there has not yet been a coherent geologic model put forward for how ice deposits have formed and evolved that can be used to assist in planning prospecting campaigns or developing relevant hardware. Here, we propose a system model for understanding these deposits at scales of meters to hectares. The model considers sources of water ice, capture at and below the surface, and retention; it focuses heavily on impact gardening as a modifying process that drives changes in how ice is distributed. 3-dimensional stochastic impact simulations are then used to test the system model and explore how ice deposits might evolve over an area the size of a potential mining outpost. The simulation results showed ice concentrations should eventually become fairly homogeneous at meter to hectare scales due to impact gardening, and high concentrations are distributed randomly rather than clustered in Earth-like ore bodies. We found the best ice deposits for extracting likely exist 10s of cm deep or more, even in locations where ice is currently stable at the very surface. Terrestrial mining software was then used to create block models and grade/tonnage curves that can inform future in-situ resource utilization demonstration missions and future mining operations planning.

1. Introduction

Water ice and other frozen volatile species are present at both poles of the Moon, within, and likely peripheral to the permanently shadowed regions (PSRs) (Feldman et al., 1998; Colaprete et al., 2010; Gladstone et al., 2012; Hayne et al., 2015; Fisher et al., 2017; Lawrence, 2017; Li et al., 2018). PSRs are those areas that never receive direct sunlight over the 18.6 year precessional cycle of the Moon (e.g., Mazarico et al., 2011) and thus have very cold surface temperatures. Future orbital missions will refine the ice detections within and around the PSRs, and landed spacecraft can study the stratigraphy of volatile-rich deposits to address currently outstanding questions about lunar history and the nature of volatiles in the solar system. More recently though, there has been a focus on the practical applications of harvesting lunar water ice as a resource to support exploration and industrialization in space (Kornuta et al., 2019; Sowers and Dreyer, 2019). After collecting and purifying water ice (hereafter, just “ice”), liquid water can be electrolyzed to produce both hydrogen and oxygen for propellant, a key enabler for operations within cislunar space, and for raising Earth satellite orbits (Lewis, 1996; Kornuta et al., 2019). The advantages of mining ice instead of extracting oxygen from lunar regolith are lower energy

requirements, simpler processing, and no need to bring the requisite hydrogen (or alternative fuel) from Earth. However, regolith is located everywhere, and ice is only found in specific locations. Preliminary studies have been carried out to address the business case for an ice mining outpost at the lunar poles (Kornuta et al., 2019; Pelech et al., 2019), and both Luxembourg and the United States have passed legislation giving their citizens and corporations ownership rights over resources mined in space, including ice on the Moon (e.g., the [Space Resource Exploration and Utilization Act of 2015](#)).

Two major limitations prevent moving forward with prospecting for and extracting lunar ice: (1) the coverage of remote sensing data and the ability to uniquely interpret it, and (2) the lack of a geologic model for ice deposit characteristics. Remote sensing using ultraviolet, visible, and near-infrared spectrometers (e.g., Hayne et al., 2015; Li et al., 2018) is limited to the very upper surface of the regolith (microns to millimeters) and will not exceed 100 m horizontal spatial resolution in the foreseeable future. Measurements using neutron spectroscopy, particularly the Lunar Prospector Neutron Spectrometer (LPNS) (Feldman et al., 1998; Lawrence et al., 2006; Elphic et al., 2007; Teodoro et al., 2010) extend approximately a meter deep, but the horizontal resolution is much coarser and therefore it is difficult to link these data to the surface ice

^{*} Corresponding author.

E-mail address: cannon@ucf.edu (K.M. Cannon).

detections. Radar measurements from the Mini-SAR and Mini-RF instruments extend meters deep with better spatial resolution, but have proved ambiguous and non-unique. Some studies have argued for thick, pure ice deposits in certain locations (Nozette et al., 2001; Spudis et al., 2013), while others set upper limits of 5–10 wt% ice mixed in the regolith (Stacy et al., 1997; Neish et al., 2011; Thomson et al., 2012). Fa and Cai (2013), and Fa and Eke (2018) have argued convincingly that radar “anomalous” craters (Spudis et al., 2013) are consistent with rocks, and not necessarily thick ice layers. The Chang’E-2 radiometer may have detected subsurface ice (Yang et al., 2019) but the concentrations and depths are not clear. Recently Rubanenko et al. (2019) used the statistics of crater depth/diameter ratios as indirect evidence for thick ice deposits in small to medium sized craters at the lunar south pole. However, these results cannot be used to pinpoint which specific craters might host these types of deposits, and have yet to have been followed up on.

In terrestrial mining, models of ore deposits are constructed based on (1) field mapping, (2) quantitative exploration results (especially drill core data), and (3) a geologic understanding of the processes that have led to initial mineralization and any subsequent modification (i.e., a concept model, or a system model; Casanova et al., 2020). These models are used to decide which mining projects are worth investing in in the first place, and for mine planning and scheduling in those cases where a project is developed (Runge, 1998). Rigorous reporting codes are used to describe the resources as exploration proceeds, as is required by law in various countries. The Joint Ore Reserves Committee (JORC) code (JORC, 2012) is one of the more well-known reporting systems, and includes terminology relating exploration results, mineral resources, and ore reserves (Fig. 1); progressing down the vertical axis of Fig. 1 is a function of “increasing level of geological knowledge and confidence”. For the Moon, the vast literature on ice detections and thermophysical modeling (as cited here) might together constitute some of the requisite geologic knowledge, but until now this information has not been put together as a coherent framework along with tools to test and validate it.

The goals of this paper are to: (1) propose a system model that captures the processes operating in and around the PSRs; (2) create regional-scale maps including ice Terrain Types and an Ice Favorability Index based on that model; (3) carry out 3-dimensional stochastic impact simulations that simulate different Terrain Types from the system model at the mining scale; and (4) define selective mining units and use the results of the simulations to create reference block models for a hypothetical ice extraction zone.

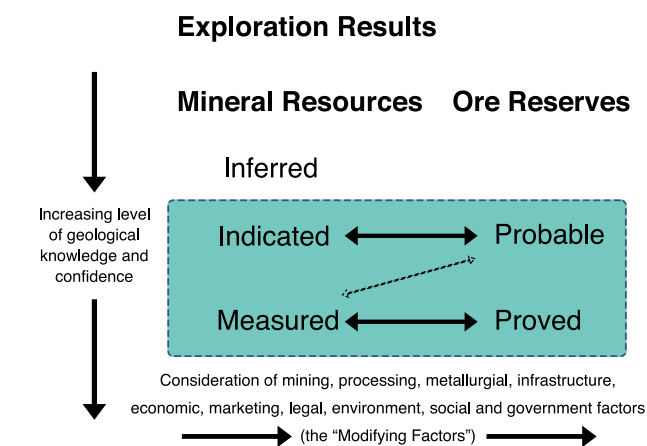


Fig. 1. Basic principles of the JORC code (reproduced from JORC, 2012). Progressing down along the vertical axis requires geologic knowledge about the resource, which is currently lacking for lunar ice.

2. System model

Here, we propose a conceptual system model for how ice deposits have formed and evolved at the lunar poles (Fig. 2). We are mostly concerned with subsurface ice like that consistent with data from neutron spectroscopy (Feldman et al., 1998; Feldman et al., 2001; Lawrence et al., 2006) and the Lunar CRater Observation and Sensing Satellite (LCROSS) experiment (Colaprete et al., 2010), which represents a greater potential resource than thin surface frosts or H₂O monolayers. As defined by Casanova et al. (2020), a system model is “a model used to represent the development of a reservoir, including the processes and critical elements associated with generating, transporting and storing the targeted resource.” Our model builds on previous work from others and attempts to strike a balance where interpretations differ; assertions made in this model are then directly explored using the 3D stochastic cratering simulations described in the following section.

2.1. Sources of ice

Three main sources are likely responsible for the majority of water ice present at the lunar poles: (1) Delivery by carbonaceous asteroids, and to a much lesser extent, comets; (2) Volcanic outgassing from the lunar interior; and (3) Solar/Earth wind implantation combined with micrometeoroid impacts. Recent efforts by Deutsch et al. (2019), Lucey et al. (2020), and Cannon et al. (2020) have begun to try and quantify the relative importance of these sources, and to assess their rates over time.

The impact flux was orders of magnitude higher between 4.5 and 3.5 Ga than from 3.5 to 0 Ga (Fig. 2; Neukum, 1983; Neukum et al., 2001

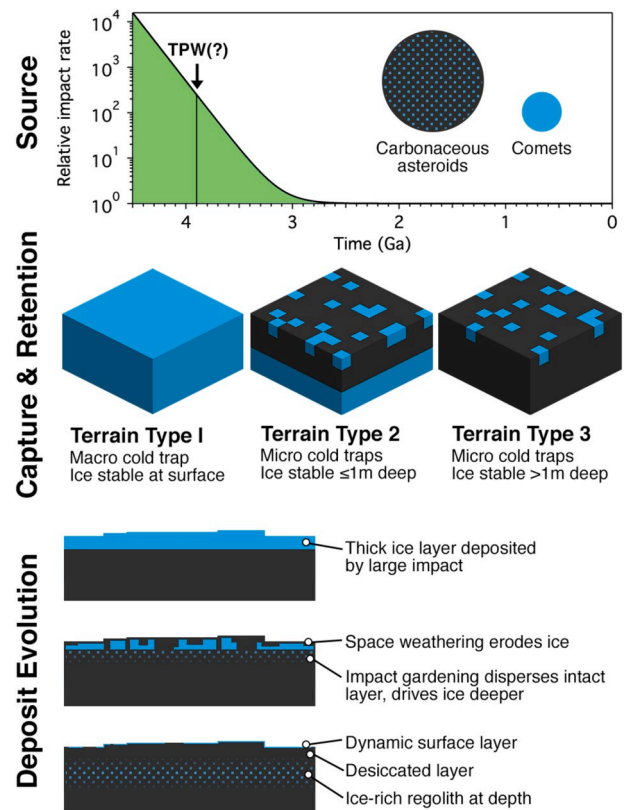


Fig. 2. System model overview. Top: impact rate over time (Neukum, 1983; Neukum et al., 2001) normalized to 1 at present, with the poorly-constrained timing of true polar wander (TPW) used in the model here. Relative sizes of asteroid and comet contributions from Ong et al. (2010). Middle: capture and retention terms determine the three Terrain Types in the system model. Bottom: schematic cross section showing evolution of polar ice deposits.

Morbidelli et al., 2018), and impacts represent a major source of volatiles that alone could account for the entire hydrogen signature detected at the poles by LPNS (Watson et al., 1961; Arnold, 1979; Ong et al., 2010; Stewart et al., 2011; Svetsov and Shuvalov, 2015; Prem et al., 2015). The smallest size fraction of impactors (<1 g) is known as micrometeoroids. If micrometeoroids contain ice and/or hydrous minerals, they can deliver volatiles directly to the lunar surface, either at the cold traps themselves or elsewhere (relying on migration). Larger volatile-rich impactors can implant water in melts and breccias and in surviving projectile fragments (Daly and Schultz, 2018) that can later be vaporized and migrate to the poles. Still-larger impacts create transient collisional atmospheres for hours to days, from which water vapor can be sequestered directly in cold traps (Ong et al., 2010; Stewart et al., 2011; Prem et al., 2015). Prem et al. (2015) calculated nonuniform ice layers of mm to cm thickness could have been deposited for a 2 km diameter pure ice impactor, and Ong et al. (2010) calculated delivery to the poles of up to 5.0×10^{14} kg H₂O from asteroids, and 7.8×10^{13} kg from comets per Ga, but using much lower present-day impact fluxes.

Volcanic outgassing is another sporadic process that was orders of magnitude more intense in the Moon's early history (Head, 1976). Needham and Kring (2017) and Needham et al. (2019) suggest intense spikes in volcanic activity at ~ 3.8 and ~ 3.5 Ga could have outgassed sufficient water vapor to create ice deposits ~ 1.5 m thick if emplaced instantaneously. This amount is again sufficient on its own to explain the neutron spectroscopy data. However, if volcanism was not as clustered as these authors propose, collisional atmospheres may not have formed to allow easy transport poleward (Wilson et al., 2019). Still, H, OH, and H₂O molecules implanted in equatorial regions could migrate to polar cold traps through ballistic transport across the lunar surface (Crider and Vondrak, 2002; Moores, 2016).

The Moon's upper surface is exposed to the space environment, including solar wind and Earth wind which can implant hydrogen in the regolith (e.g., Crider and Vondrak, 2000; Starukhina and Shkuratov, 2000; Wang et al., 2019). Crider and Vondrak (2003a) calculated the combined effects of space weathering processes including solar wind implantation to be net depositional of H₂O in cold traps, reaching a steady state concentration of ~ 4 wt% ice within the regolith column. However, additional processes are required to go from H, to OH and H₂O (Zeller et al., 1966), potentially limiting the potency of solar/Earth wind as an ice source. As noted by Zhu et al. (2019), micrometeoroids may be crucial for driving these reactions. The contribution of wind-delivered hydrogen is a function of solar activity over time: Airapetian and Usmanov (2016) and Pognan et al. (2018) modeled the long-term history of solar wind, finding its velocity and density should have been much higher early in solar system history. At face value, this suggests a decrease in the source over time, similar to impact- and volcanic-derived volatile sources.

In our system model, we consider impact delivery to be the dominant mechanism by which thick layers of ices were emplaced at the surface of cold traps and worked down into the regolith before erosive forces removed the ice. Volcanic outgassing could have formed thick layers under unique circumstances (Needham and Kring, 2017), and solar/Earth wind-based delivery likely only formed thin, transient layers that were highly vulnerable to removal (Zimmerman et al., 2013; Farrell et al., 2019). Because impacts were a much more significant source of ice early in the Moon's history (4.5–3.5 Ga) than afterward, older surfaces have received a greater cumulative supply of ice than younger ones, with a strong uptick between about 3.0–3.5 Ga (Fig. 2).

2.2. Ice capture at the surface and at depth

For ice deposits to build up at the lunar poles, there must have been effective trapping mechanisms at work. In our system model, we distinguish between two primary types of cold traps: (1) macro cold traps ($>10^4$ m²), in which an entire region is cold enough to effectively trap incident water ice at the surface, and (2) micro cold traps ($<10^4$

m²), in which rough terrain in an otherwise illuminated region creates small areas that can trap ice (Fig. 2). The macro cold traps are more or less synonymous with the classically defined PSRs: those mapped by Mazarico et al. (2011) and Kloos et al. (2019). These include large craters like Haworth and Sverdrup at the south pole, and smaller dispersed PSRs more typical at the north pole. Outside of the PSRs, rough topography creates micro cold traps that function the same way on a smaller scale (Rubanenko and Aharonson, 2017). This phenomenon is latitude-dependent, and Rubanenko and Aharonson (2017) predict a ~ 5 – 15% areal fraction of micro cold traps for polar regions above 80° latitude. Kloos et al. (2019) and Williams et al. (2019) highlighted the importance of seasonally shadowed regions (SSRs): areas that can trap ice but only during parts of the lunar orbit. This greatly expands the area where ice can be captured, but retaining ice in these SSRs is likely to be an issue (see below). Another capture mechanism is the “ice pump” described by Schorghofer and Aharonson (2014), in which a narrow set of temperature conditions allows ice to diffuse down into the regolith column after being cold trapped at the surface. However, the authors note the efficiency of this process may be limited.

2.3. Ice retention and disruption

Retaining ice on geologic timescales is a prerequisite for developing deposits that can be extracted today. In past studies, stability of ice within the regolith column has been calculated based on sublimation timescales using thermophysical models (Zhang and Paige, 2010; Paige et al., 2010; Siegler et al., 2016). Ice is calculated to be stable at the very upper surface in PSRs, and at greater depths buried under insulating regolith in surrounding areas. In our system model, we define three Terrain Types (TT) based on ice capture and retention (Fig. 2): Terrain Type 1 (macro cold trap, ice stable at 0 m depth), Terrain Type 2 (micro cold traps, ice stable at ≤ 1 m depth), and Terrain Type 3 (micro cold traps, ice stable at >1 m depth). This division is based on: (1) natural breaks in the ice stability depth histograms at 0 m and around 1 m (Siegler et al., 2016), and (2) a change in strategies for prospecting and extracting water ice. For example, infrared and microwave heating may be effective for liberating volatiles from regolith in TT1 and TT2 regions, but not TT3 where ices are likely located deeper down.

Thermophysical models calculate stability against sublimation only, and Farrell et al. (2019) recently challenged the concept of ice stability at the surfaces of cold traps, calculating that surface ice layers can only persist for thousands of years rather than billions due to space weathering effects. It remains unclear how a dynamic and possibly transient surface ice layer relates to deeper diffuse ice inferred from LCROSS, LPNS, and the Chang'E-2 radiometer (Colaprete et al., 2010; Feldman et al., 1998; Yang et al., 2019), particularly if a desiccated regolith layer separates the two reservoirs (Feldman et al., 2001; Lawrence et al., 2006; Benna et al., 2019). However, as mentioned above we are interested here in greater depths than those affected by space weathering processes at the very surface.

After thick layers of ice were deposited, ice distributions at centimeter to meter depths were modified mostly by impact gardening, the constant impact-induced churning and overturn of the regolith dominated by impact secondaries (Gault et al., 1974; Costello et al., 2018; Costello et al., 2020). We consider impacts to be the most important geologic process at these scales (i.e., larger than space weathering scales), given the lack of major volcanic provinces near the lunar poles, and the modest expected effects of lunar tectonism. Impact-driven mixing would have been especially intense prior to ~ 3 Ga, and had a number of effects on deposited ice. First, any pure ice layers would be punctured and comminuted. Some of the ice was vaporized by each impact: a small fraction would be re-deposited nearby due to the cold trap effect, but most vapor achieved sufficient velocity to escape the cold trap or the Moon itself (Farrell et al., 2013; Farrell et al., 2019). Non-vaporized ice was pushed down and out in the displaced zones (see Fig. 5) of crater transient cavities (Grieve and Garvin, 1984; Osinski

et al., 2011), such that it was mixed into underlying dry regolith. Both dry and icy regolith in crater excavation zones (see Fig. 5) were brought to the surface, creating a complex stratigraphy of intercalated rock grains (mostly anorthosite at the poles) and ice grains. Over time, ice that was originally deposited at the surface would extend deeper, become more diluted with dry regolith, and the regolith column would become better mixed vertically (Costello et al., 2018, 2020); horizontal mixing could have also emplaced ice at depth in nearby areas where it was not stable at the surface. Impact-induced seismic shaking would have compacted icy regolith deposits at depth, as it does elsewhere on the Moon (Schultz and Gault, 1975; Richardson et al., 2004). Near the upper surface, vaporization and re-deposition could have created icy agglutinates similar to their glassy counterparts (McKay et al., 1974), but regolith in PSRs was unlikely to have been cemented like permafrost because of continued impact gardening.

2.4. Complications: obliquity and true polar wander

The present-day lunar obliquity and spin-axis pole locations may not have been the same over geologic time, which could complicate the history of ice deposition and stability (Sieglar et al., 2015; Sieglar et al., 2016). Sieglar et al. (2016) have presented compelling evidence the Moon underwent ~5.5° of true polar wander in its ancient history (~4 Ga), shifting the places where ice could be captured and retained. In Fig. 3, we consider the consequences of such a shift on the three Terrain Types described above. For surfaces that formed prior to true polar wander, there are 9 different permutations in the evolution of Terrain Types that we map out over the poles (Fig. 3e,f). These can be distinguished by extending our nomenclature, for example TT1 → 3 represents a region that changed from TT1 to TT3 after true polar wander. Regions where ice was stable at the surface at both the paleo and present pole (TT1 → 1) should be most favorable for developing and retaining rich ice deposits, but very few locations actually satisfy this condition (<1% of

the area from 80 to 90° latitude). Additionally, these regions are deep inside large, steep-walled craters and may only be accessible with nuclear-powered architectures.

2.5. Ice Favorability Index

By combining the different aspects of the system model together (Figs. 2,3), we generated regional-scale maps of what we call an Ice Favorability Index (IFI). The index is based on a source term (§2.1), a capture term (§2.2), and a retention term (§2.3); locations where any of these aspects are lacking or deficient were not likely to have accumulated deep, substantial deposits of ice that persist to the present day. The mathematical formulation of the IFI is described in detail in Appendix A, and Fig. 4 shows the IFI over both lunar poles.

In terms of ice favorability, two regions of interest are notable at the south pole. Cabeus crater, the site of the LCROSS impact, has some of the highest IFI values of any location at the poles (Fig. 4). This is a consequence of the ancient age of Cabeus, and it having large areas of macro cold traps and near-surface ice stability both at the paleopole and present-day pole. At face value, these IFI values suggest the modeled LCROSS water amounts at Cabeus (~5%; Colaprete et al., 2010) may be a reasonable conservative estimate for the maximum amount of ice to be

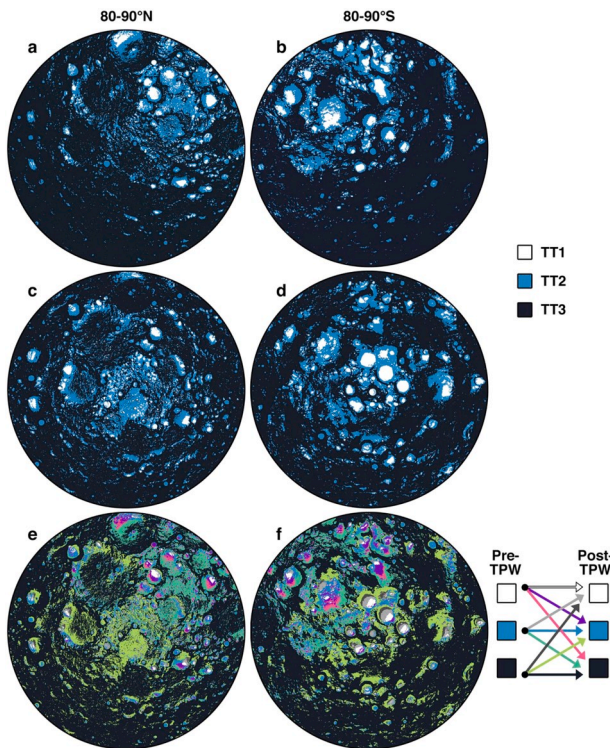


Fig. 3. Classification of polar regions based on the three Terrain Types in our system model (Fig. 2). a) North paleo pole; b) South paleo pole; c) North present pole; d) South present pole; e) North combined (see arrows for color coding); f) South combined.

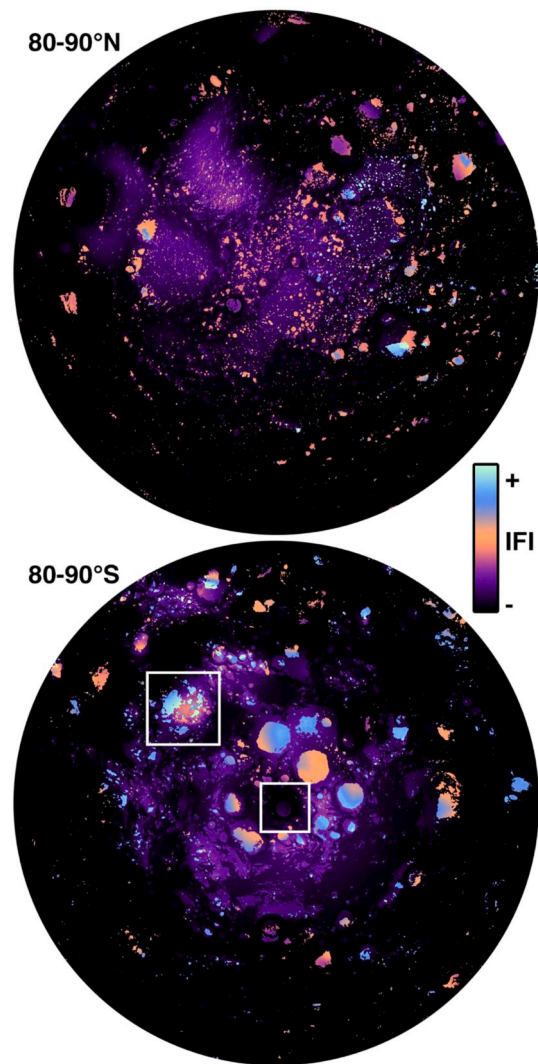


Fig. 4. Ice Favorability Index (IFI) for the north pole (top) and south pole (bottom), from 80 to 90° latitude. Boxes over the south pole show locations of Cabeus crater (upper left) and Shackleton crater (lower right) discussed in the text.

expected in regional-scale polar deposits. On the other hand, Shackleton crater has some of the lowest IFI values of any PSR at the south pole (Fig. 4). This results from its very young relative age, and the fact that Shackleton was not a PSR at the paleopole location of Sieglar et al. (2016). Also of note are substantial areas of elevated IFI outside the PSRs themselves, where ice could have been captured in micro cold traps and may be found at shallow depths within the regolith column.

3. 3-Dimensional cratering simulations

3.1. Simulation description

The system model above outlines the major geologic processes operating to deposit and modify ice, and delineates regional-scale Terrain Types and predicted ice favorability (Figs. 3,4). To first order, impact gardening is the most significant process involved: to get a better sense of how it affects ice distributions at local scales (meters to hectares), we constructed computer-based 3D stochastic cratering simulations. These simulations build on pioneering work by Crider and Vondrak (2003a, 2003b) and Hurley et al. (2012) that modeled a 1D column, or a pair of columns, including space weathering and impact effects. New advances here include a 3D grid, a larger vertical depth scale, the geometry of macro vs. micro cold traps, and different ice stability depths.

Our simulations consist of a square grid of $500 \times 500 \times Z$ cells representing a 0.25 km^2 area at the lunar poles, with a horizontal resolution of 1 m and a vertical resolution of 0.1 m. This area is a reasonable size for a small to medium-sized mining outpost. Each grid cell has a fractional value representing its ice content in weight percent. For the initial simulations described here, we began with a pure ice layer on top of completely dry regolith, as might be emplaced by a large impact event (Prem et al., 2015).

Impact gardening was modeled in two ways: craters with diameters between 20 and 100 m were modeled explicitly using a constant production function from Ivanov et al. (2001), with crater locations placed randomly on the grid. These larger craters (still small by lunar standards) were modeled with depth/diameter ratios of 0.2 (Pike, 1974), and transient cavity diameters (D_{tc}) of $0.84D$, where D is the final crater diameter (Melosh, 1989). Ejecta lobes (Fig. 5) extend down to $0.1D_{tc}$ (Melosh, 1984), and material within these lobes is ejected out to 1 crater diameter away, with ejecta thickness falling off as $0.14R^{0.74}(r/R)^{-3.0}$ where R is the crater radius and r is the radial distance from the crater center (McGetchin et al., 1973). The shallowest material is ejected furthest, consistent with cratering physics (e.g., Osinski et al., 2011). Material within the ejecta blankets is not mixed together, but can be mixed by smaller-scale gardening (described below). Beneath the ejected zone, material in the displaced zone is pushed downwards. In this way of moving grid cells around, the simulations capture the 3D effects of hollowed out craters with realistic ejecta deposits. Results from the Costello et al. (2018) model were parameterized to account for gardening from smaller craters that cannot be resolved on an individual basis. To do this, grid cell values are averaged together in a depth-dependent fashion: the upper 10 cm is fully homogenized, the upper ~ 50 cm is partially mixed, and the upper ~ 1.5 m is well mixed, all on 1 Ga timescales (Costello et al., 2018). Minton et al. (2019) studied the detailed effects of small crater destruction, finding that distal ejecta fragments in crater rays are the main driver of diffusive degradation. Our simulations include cookie cutting and ejecta burial effects, but not heterogeneous rays and distal mixing effects (Huang et al., 2017; Minton et al., 2019). We added a parameterized version of linear diffusive erosion that softens the topography, with an erosion rate of 0.4 mm/Myr (Fassett and Thomson, 2014). However, detailed distal mixing effects are beyond the scope of the present work.

The cratering simulations were first tested using a macro cold trap scenario (TT1), then modified to represent the other two Terrain Types from Fig. 2. In the TT1 scenario, the simulation began with a 10 cm thick

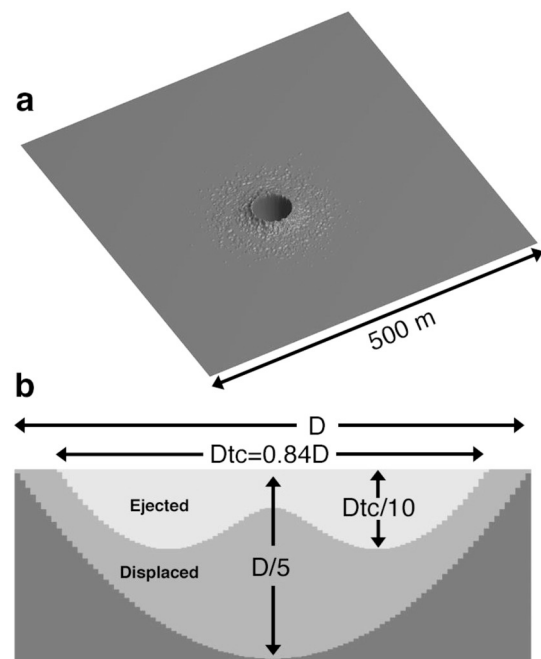


Fig. 5. Parameterization of craters in the 3D simulations. a) Oblique view of simulation grid with a 50 m diameter impact crater showing the topographic effects including ejecta (vertically exaggerated). b) Cross section showing the relative dimensions of the ejected and displaced zones for each larger crater in the simulations.

layer of pure ice over the entire grid surface, with ice stable throughout the regolith column. 3.5 Gya of gardening (present-day flux) was simulated with a timestep of 10^5 years. For the micro cold trap scenarios, the upper surface was instead seeded with a 5% areal fraction of cold traps, each starting with 10 cm of pure ice. The ice stability depth increased linearly away from those surface cold trap locations such that 40% of the grid had subsurface cold trap areas (Rubanenko and Aharonson, 2017). For the Terrain Type 2 scenario, the ice stability depth outside these cold traps was set at 50 cm deep (halfway between the 0 and 1 m bounds), and in Terrain Type 3 it was set at infinite depth. In these two latter scenarios, we kept the cold trap locations fixed in place over time; this is not physically realistic, because in reality impacts will both destroy existing micro cold traps and create new ones in the resulting craters. However, this level of detail is outside the scope of the present work for a model with hundreds of individually resolved impacts.

There are a large number of free parameters and unknowns in the cratering simulations, so we chose to focus on a relatively simple configuration: pure ice on top of dry regolith, subjected to impact gardening. Future work will incorporate added complexity, for example stochastic ice deposition events, and changes in ice stability depth during the simulations. However, we do not expect the basic behavior to change in those more complicated scenarios. The outputs of the simulations here are given in absolute concentrations of ice (wt%), but the real significance is not these quantitative values but the changes observed over time, the resulting ice distributions, and the relative differences between different runs with all other variables held constant.

3.2. Simulation results

The simulations generally evolved according to the expected effects of impact gardening described above. Fig. 6 shows how the upper surface of the grid evolved as a function of time for the Terrain Type 1 scenario. Large impact craters excavated dry regolith from beneath the upper ice layer and emplaced it on the surface, while the small-scale

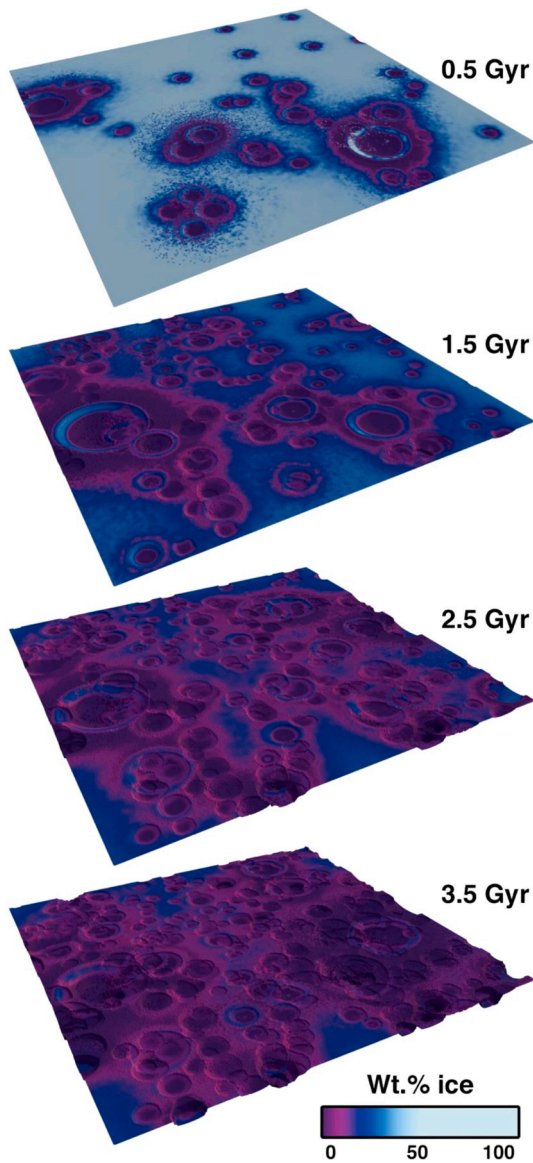


Fig. 6. Stochastic cratering simulation results for the TT1 configuration. Oblique view showing the very upper surface of the model grid.

parameterized gardening slowly homogenized dry and icy material, diluting the ice concentrations. After 3.5 billion years, the end result was a patchy surface distribution of ice, with most concentrated areas being those that had not yet been affected by the larger craters, or in some cases in the walls of larger craters (Fig. 6). Fig. 7a shows this same time evolution but as a function of depth. The plots show ice being driven deeper over time, becoming more homogeneous as a function of depth, and the maximum ice concentration shifting deeper. All these behaviors are predicted effects of impact gardening on a surface layer of pure ice.

Significant differences were observed between the three different Terrain Types, and these differences can be linked to varying efficiencies of ice capture and retention. Fig. 7b shows the final mean ice concentration as a function of depth for the three different simulation scenarios. All three scenarios show an increase in ice concentration to a maximum located about 50–100 cm deep, where it then falls off again toward deeper depths. The Terrain Type 1 simulation had significantly higher ice concentrations at all depths, due to the increased cold trap area and ice being stable throughout the regolith column over the entire grid. Terrain Type 2 had moderately greater ice concentrations than Terrain Type 3, due to the ice stability depths being comparatively higher in the

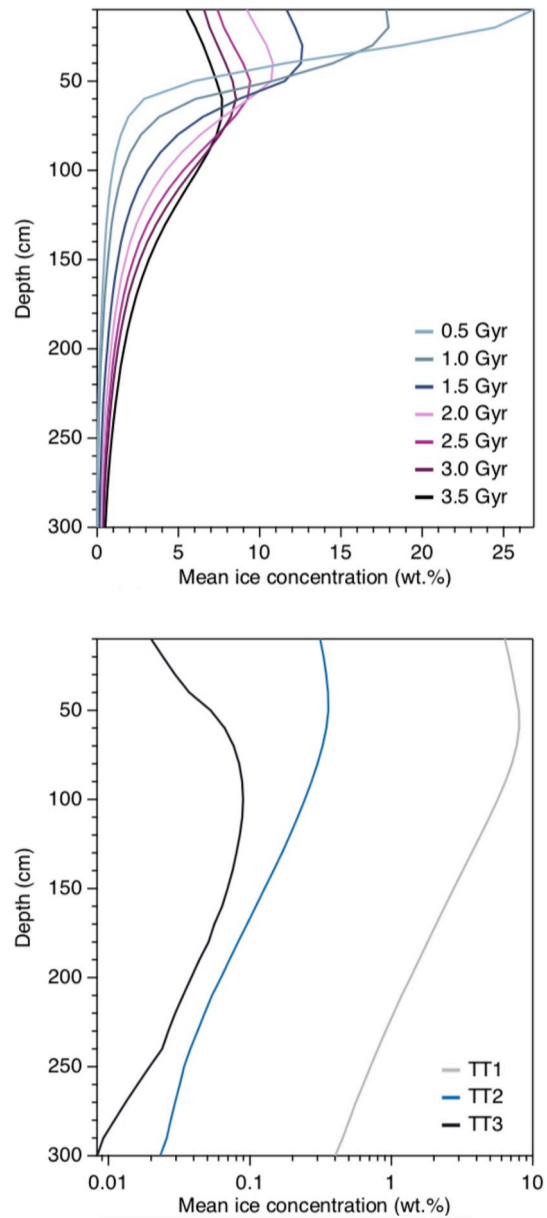


Fig. 7. Top: Changes in mean ice content (averaged horizontally) over time in the stochastic cratering simulations for the Terrain Type 1 scenario. Bottom: Comparison of results for all three Terrain Types (note log scale).

regolith column: this allowed more ice mixed down by large craters to be retained over time. For similar reasons, the maximum of the ice concentration curve occurred deeper in the regolith column for Terrain Type 3.

3.3. Selective mining units and grade/tonnage models

In terrestrial mining, a selective mining unit (SMU) is the smallest volume of material that can be classified as ore or waste, and we applied this concept to the stochastic cratering simulation results. Based on proposed architectures for ice mining at the lunar poles, we propose two different SMU sizes: a $1 \times 1 \times 0.1$ m ($w \times l \times h$) volume for drilling/excavation-based methods, and a $10 \times 10 \times 1$ m volume for methods based on heating with volatile capture tents (Sowers and Dreyer, 2019). We exported the cratering simulation results into the terrestrial mining software Leapfrog Geo, then produced block models and grade/tonnage curves based on the $10 \times 10 \times 1$ m SMU. Fig. 8 shows the resulting block

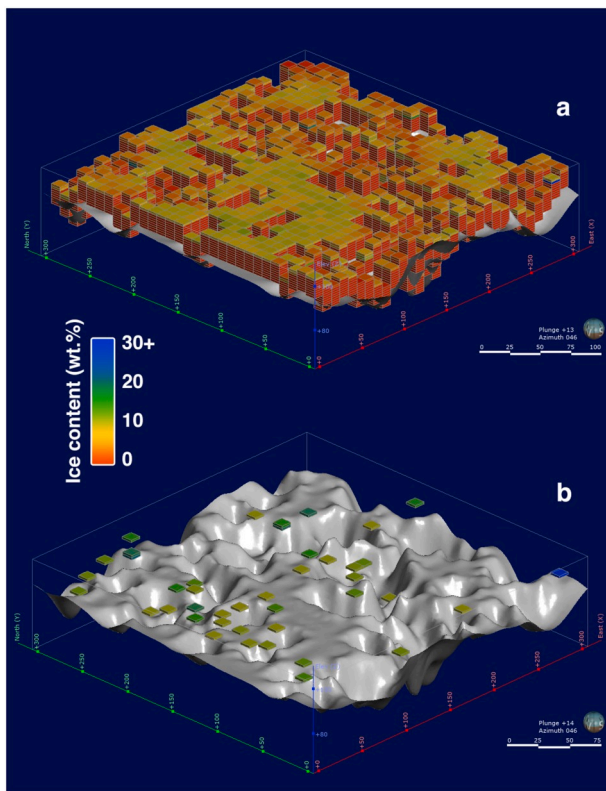


Fig. 8. Block model of the TT1 simulation (cropped to the inner 300×300 m) with a block size of $10 \times 10 \times 1$ m. a) All blocks shown. b) Only high-yield (>15 wt% ice) blocks are shown. As can be seen, there are no large coherent “ore bodies” of high-yield ice deposits.

model from the Terrain Type 1 simulation, and Fig. 9 shows its grade/tonnage curves. In Fig. 8b, we filtered the block model to only include the highest concentration ice deposits (>15 wt% in this case). As is seen, these high-yield blocks are randomly distributed instead of being clustered into “ore bodies”, and this has significance for prospecting strategies discussed further below. It remains to be seen what ice concentration will prove economical to extract, but based on that cutoff grade, the types of curves in Fig. 9 can be used to estimate total yields from a given volume of regolith. The block models for the three Terrain Type scenarios are included as CSV files in the Supplementary Material, and these can be used as reference cases to plan mining efforts.

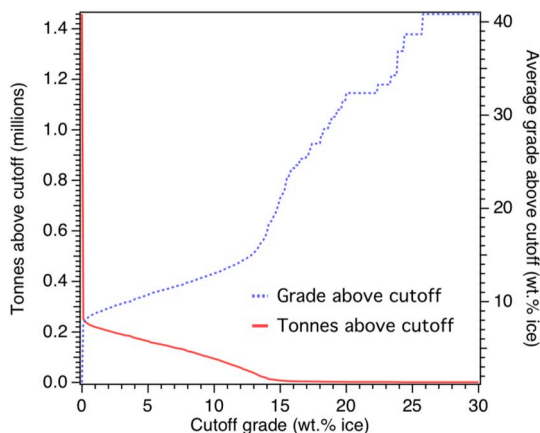


Fig. 9. Grade/tonnage curves from the block model generated for the TT1 simulation run (Fig. 8).

4. Discussion

The system model and simulations described here cannot be used to predict quantitative ice concentrations or stratigraphies for specific locations on the Moon, but some general trends are apparent and have practical implications for both prospecting, and mining hardware design. Some of these trends are more intuitive than others, and have been noted by previous authors (e.g., Hurley et al., 2012).

4.1. Deeper is better

In all three Terrain Types, the highest average ice concentrations in the simulations occurred at some depth below the surface, at least 50 cm (Fig. 7b). This was observed even where ice was stable at the upper surface, and is caused by the depth-dependent efficiency of impact gardening combined with surface deposition of ice. Gardening is more effective at shallow depths because smaller impacts are more abundant, and pockets of highly concentrated ice close to the surface will quickly be homogenized with excavated dry material. As well, erosive space weathering processes not included in the simulations (sublimation, sputtering, etc.) occur at the upper surface of cold traps, and this should increase the rate at which a desiccated layer develops. The upper dry layer observed in the simulations is consistent with the favored 2-layer dry over wet model from neutron spectroscopy observations (Feldman et al., 2001; Lawrence et al., 2006) and a centimeters-thick desiccated layer inferred from LADEE data (Benna et al., 2019). We expect higher impact gardening rates early in the Moon’s history would have led to even faster-formed, and potentially deeper desiccated surface layers. However, this was balanced against larger and more closely spaced volatile-bearing impacts.

4.2. Motherlode (or not)

Many informal discussions about lunar ice mining are centered on the idea of finding spatially coherent ore bodies of ice by a 1:1 analogy to hard rock deposits on Earth. Prospecting is envisioned as mapping their boundaries with extensive campaigns using neutron spectroscopy or drilling. This may be a misguided approach if impact gardening is the major process affecting ice deposit characteristics, as it probably has been. Gardening will eventually lead to more homogeneous ice distributions at all spatial scales, and enriched ice pockets observed in the simulations were randomly located (Fig. 8b). No large, coherent “ore bodies” were seen. With an initial surface layer of ice 10 cm thick, our simulations ended up with low amounts of ice (mean of 1.2, 0.04, and 0.01 wt% for TT1, TT2, and TT3, respectively) throughout the regolith column, with no thick coherent layers remaining.

4.3. Local geologic features are important

Impact craters can be mapped at meter to ten-meter scales using high-resolution stretched NAC images, or LOLA hillshade data, over potential mining sites. If, as in our system model, ice was originally emplaced at the upper surface of a cold trap then gardened by impacts, the results in Figs. 6 and 8 suggest intercrater plains are generally more favorable for hosting ice than the ejecta/rims/floors of small craters because the initial ice layer has not been disrupted by impacts. This is fortuitous because small craters represent trafficability hazards anyway. However, for more ancient terrains, it may not be possible to find areas unaffected by significant gardening.

4.4. There may be an optimum surface age for ice deposits

For two surfaces with the same initial ice supply, the younger (less gardened) surface will be generally more favorable for mining because the ice should be less thoroughly mixed into the regolith column (Fig. 7). However, H_2O supply rates from impacts and volcanism sharply

declined until plateauing at their current values around 3.0 Ga (Fig. 2). Therefore, younger craters like Shackleton are probably not ideal for mining because of a lack of supply, and there may be an optimum surface age that balances increased supply (good) with increased exposure to gardening (generally bad).

5. Conclusions

Water ice and other volatile species have been deposited at the lunar poles and then modified by a variety of processes. Here, we presented both a conceptual system model for how these deposits have evolved at regional scales, and 3D cratering simulations for a local area the size of a potential mine site. We consider impact cratering, specifically smaller-scale gardening, to be the major process affecting subsurface ice distribution: over time, gardening should lead to lower overall ice concentrations, deeper deposits, and increased homogeneity. Based on cold trap sizes and ice stability depths, we defined and mapped three different Terrain Types and carried out simulated gardening in each of them. The simulation results showed a favorability of Terrain Type 1 > 2 > 3, as expected, and that the best deposits are likely located at modest depths (10s of cm) below the surface. However, complicating factors include a decrease in the supply of ice to the poles over time, the specific

timing of true polar wander, and the formation of large craters that would have buried older ice deposits in thick layers of ejecta. Finally, we used terrestrial mining software to create block models for the modeled scenarios, and include these data to use as reference cases for planning lunar mining architectures. These models provide a testable framework that can guide the next generation of lunar prospecting missions.

Declaration of competing interest

The authors declare that they have no known competing financial interests or personal relationships that could have appeared to influence the work reported in this paper.

Acknowledgements

We would like to thank Matt Siegler for providing the ice stability depth data used here, and Emily Costello for helpful discussions. Comments from two anonymous reviewers greatly improved the content of the manuscript. This work was directly supported by NASA's Solar System Exploration Research Virtual Institute cooperative agreement notice 80NSSC19M0214 for the Center for Lunar and Asteroid Surface Science (CLASS).

Appendix A. Ice Favorability Index

The Ice Favorability Index (IFI) is a unitless measure meant to predict which locations at the lunar poles may be more or less favorable for hosting deep, substantial deposits of water ice. It is not meant to be a quantitative measure of ice resources or reserves, and should not be used in isolation to select landing sites or mining locations. The intent of the IFI is to guide further site analysis and ground prospecting efforts.

The main inputs into the model are the ice stability depth maps from Siegler et al. (2016), the latitude-dependent micro cold trap areal fractions from Rubanenko and Aharonson (2017), the impact flux over time from Neukum (1983) and Neukum et al. (2001), and an estimate for the crater retention age of a location using the Robbins (2019) crater database. In this iteration (version 1), the IFI is created on a stereographic grid from 80° to the pole, 1000 × 1000 cells in size, with a horizontal resolution of ~532 m/cell.

A.1. Ice stability depth maps

These maps are available either from the NASA Planetary Data System or from the authors of Siegler et al. (2016). They provide a modeled depth in the regolith column where water ice is stable against sublimation on billion-year timescales. These ice stability depth (ISD) values range from ice stable at the upper surface, to ≥2.5 m deep. We used maps for both the proposed paleopoles of Siegler et al. (2016), as well as the present-day poles.

A.2. Latitude-based cold trap area

Rubanenko and Aharonson (2017) calculated the fractional areas of micro cold traps both at the surface (A_{SURF}) and in the subsurface (A_{SUB}) as a function of latitude. We digitized the plots from their paper to calculate cold trap areal fractions using the $\sigma_s = 15^\circ$ cases (roughness on ~10 m scales). 3rd degree polynomial fits were calculated with the following coefficients:

$$A_{SURF} = 9.985 \times 10^{-5}x^3 - 0.02231x^2 + 1.663x - 41.32 \quad (1)$$

$$A_{SUB} = -4.925 \times 10^{-5}x^3 + 0.01305x^2 - 1.108x + 30.53 \quad (2)$$

Where A is the cold trap areal fraction and x is latitude in degrees.

A.3. Impact flux

We assume impact delivery is the major source of volatiles, and we used the time-dependent crater chronology function given by Neukum (1983) and Neukum et al. (2001):

$$N(1) = 5.44 \times 10^{-14}[\exp(6.93T) - 1] + 8.38 \times 10^{-4}T \quad (3)$$

where $N(1)$ is the number of craters greater than or equal to 1 km diameter per km², and T is the crater accumulation time in Gyr. The relative cratering rate over time is the derivative of this function:

$$\frac{dN}{dT} = 3.76992 \times 10^{-13}[\exp(6.93T)] + 8.38 \times 10^{-4} \quad (4)$$

A.4. Crater retention age

In order to account for time-varying deposition of ice, we need an estimate of when a given surface formed, or was last resurfaced, and therefore how long it has been a receptacle for ice delivered to the polar regions. We used a moving-window approach to count craters at every location at the poles to derive complete model age maps. To do this, we used the lunar crater database of Robbins (2019) which contains the locations and sizes of every crater >1–2 km in diameter. We rastered an aperture over the grid, and counted all craters in each aperture in 6 different size bins: 1, 2, 4, 8, 16, and 32 km. These crater counts were then converted to model ages by performing best fits to the Neukum isochrons (Neukum, 1983) with the updated constants from Ivanov et al. (2001) at 0.1 Gyr intervals. The modeled age for each grid cell is the mean of the model ages for all apertures that covered that cell.

A.5. IFI calculation

The main IFI calculation is a multiplication of three terms:

$$IFI = Source \times Capture \times Retention$$

The *Source* term describes the amount of ice available to be captured based on the age of a location and the relative cratering rate; the *Capture* term describes the ability of a surface to trap ice based on the areal fraction of that surface comprised of cold traps; the *Retention* term describes the ability of a location to sustain ice at depth based on the subsurface cold trap areal fraction and the ice stability depth.

However, true polar wander creates a complicating factor, in that the *Capture* and *Retention* terms must be computed twice: once for the paleopole (PAL) and once for the present-day pole (PRE). We do so by defining the fraction of total ice deposited before true polar wander (TPW) as f_{TPW} , such that:

$$IFI = f_{TPW}(Source_{PAL} \times Capture_{PAL} \times Retention_{PAL}) \\ + (1 - f_{TPW})(Source_{PRE} \times Capture_{PRE} \times Retention_{PRE})$$

And the appropriate paleopole and present-day pole ISD maps are used accordingly. The f_{TPW} parameter depends on the timing of the TPW event. In this iteration of the IFI, we found that placing TPW at ~3.9 Ga provided the best match between IFI and the epithermal neutron suppression maps in Sieglar et al. (2016), which gives $f_{TPW} = 0.66$.

A.6. Source terms

To calculate the $Source_{PAL}$ term, we integrated Eq. (4) from the modeled age of each grid cell until TPW. $Source_{PAL} = 0$ for those cells younger than the age of TPW. $Source_{PRE}$ was calculated by integrating (4) from either TPW or the modeled age (whichever is younger) until present-day. Both $Source_{PAL}$ and $Source_{PRE}$ were normalized to a maximum value of 1 by dividing values for all cells by the value for the oldest cell in the grid.

A.7. Capture terms

The *Capture* terms are straightforward to calculate:

$$Capture = \begin{cases} 1 & \text{if ice stable at surface} \\ A_{SURF} & \text{otherwise} \end{cases}$$

A.8. Retention terms

The *Retention* terms deal with the subsurface only. They are calculated by:

$$Stability = A_{SUB} + (1 - A_{SUB}) \times ISD_N$$

where ISD_N is the ISD renormalized to range between 1 (ice stable at the surface) to 0 (ice stable ≥ 2.5 m).

References

- Airapetian, V.S., Usmanov, A.V., 2016. Reconstructing the solar wind from its early history to current epoch. *ApJ* 817, L24.
- Arnold, J.R., 1979. Ice in the lunar polar regions. *J. Geophys. Res.* 84 (B10).
- Benna, M., Hurley, D.M., Stubbs, T.J., Mahaffy, P.R., Elphic, R.C., 2019. Lunar soil hydration constrained by exospheric water liberated by meteoroid impacts. *Nat. Geosci.* 12, 333–338.
- Cannon, K.M., Deutsch, A.N., Head III, J.W. 2020. Stratigraphy of Ice and Ejecta Deposits at the Lunar Poles. 51st Lunar Planet. Sci. Conf., Abstract #1488.
- Casanova, S., Espejel, C., Dempster, A., Caprarelli, G., Anderson, R.C., Saydam, S., 2020. Lunar polar water resource exploration—examination of the lunar cold trap reservoir system model and introduction of Play-based Exploration (PBE) techniques. *Planet. Space Sci.* 180, 104742.
- Colaprete, A., Schultz, P., Hledmann, J., Wooden, D., Shirley, M., Ennico, K., Hermaly, B., Marshall, W., Ricco, Antonio, Elphic, R.C., Goldstein, D., Summy, D., Bart, G.D., Asphaug, E., Korycansky, D., Landis, D., Sollitt, L., 2010. Detection of water in the LCROSS ejecta plume. *Science* 330, 463.
- Costello, E.S., Ghent, R.R., Lucey, P.G., 2018. The mixing of lunar regolith: vital updates to a canonical model. *Icarus* 314, 327–344.
- Costello, E.S., Ghent, R.R., Hirabayashi, M., Lucey, P.G., 2020. Impact gardening as a constraint on the age, source, and evolution of ice on Mercury and the Moon. *J. Geophys. Res. Planets* 125, e2019JE006172 (in press).
- Crider, D.H., Vondrak, R.R., 2000. The solar wind as a possible source of lunar polar hydrogen deposits. *J. Geophys. Res. Planets* 105 (26), 773–26,782.
- Crider, D.H., Vondrak, R.R., 2002. Hydrogen migration to the lunar poles by solar wind bombardment of the Moon. *Adv. Space Res.* 30, 1869–1874.
- Crider, D.H., Vondrak, R.R., 2003a. Space weathering effect on lunar cold trap deposits. *J. Geophys. Res. Planets* 108, 5079.
- Crider, D.H., Vondrak, R.R., 2003b. Space weathering of ice layers in lunar cold traps. *Adv. Space Res.* 31, 2293–2298.
- Daly, R.T., Schultz, P.H., 2018. The delivery of water by impacts from planetary accretion to present. *Sci. Adv.* 4, eaar2632.
- Deutsch, A.N., Head III, J.W., Neumann, G.A., 2019. Analyzing the ages of south polar craters on the Moon: implications for the sources and evolution of surface water ice. *Icarus* 336, 113455.

- Elphic, R.C., Eke, V.R., Teodoro, L.F.A., Lawrence, D.J., Bussey, D.B.J., 2007. Models of the distribution and abundance of hydrogen at the lunar south pole. *Geophys. Res. Lett.* 34, L13204.
- Fa, W., Cai, Y., 2013. Circular polarization ratio characteristics of impact craters from mini-RF observations and implications for ice detection at the polar regions of the Moon. *J. Geophys. Res. Planets* 118, 1582–1608.
- Fa, W., Eke, V.R., 2018. Unravelling the mystery of lunar anomalous craters using radar and infrared observations. *J. Geophys. Res. Planets* 123, 2119–2137.
- Farrell, W.M., Hurley, D.M., Hodges, R.R., Killen, R.M., Halekas, J.S., Zimmerman, M.I., Delory, G.T., 2013. Redistribution of lunar polar water to mid-latitudes and its role in forming an OH veneer. *Planet. Space Sci.* 89, 15–20.
- Farrell, W.M., Hurley, D.M., Poston, M.J., Hayne, P.O., Szalay, J.R., McLain, J.L., 2019. The young age of the LAMP-observed frost in lunar polar cold traps. *Geophys. Res. Lett.* 46, 8680–8688.
- Fassett, C.I., Thomson, B.J., 2014. Crater degradation on the lunar maria: topographic diffusion and the rate of erosion on the Moon. *J. Geophys. Res. Planets* 119, 2255–2271.
- Feldman, W.C., Maurice, S., Binder, A.B., Barraclough, B.L., Elphic, R.C., Lawrence, D.J., 1998. Fluxes of fast and epithermal neutrons from lunar prospector: evidence for water ice at the lunar poles. *Science* 281, 1496–1500.
- Feldman, W.C., Maurice, S., Lawrence, D.J., Little, R.C., Lawson, S.L., Gasnault, O., Wiens, R.C., Barraclough, B.L., Elphic, R.C., Prettyman, T.H., Steinberg, J.T., Binder, A.B., 2001. Evidence for water ice near the lunar poles. *J. Geophys. Res. Planets* 106, 23231–23251.
- Fisher, E.A., Lucey, P.G., Lamelin, M., Greenhagen, B.T., Siegler, M.A., Mazarico, E., Aharonson, O., Williams, J.-P., Hayne, P.O., Neumann, G.A., Paige, D.A., Smith, D. E., Zuber, M.T., 2017. Evidence for surface water ice in the lunar polar regions using reflectance measurements from the Lunar Orbiter Laser Altimeter and temperature measurements from the Diviner Lunar Radiometer Experiment. *Icarus* 292, 74–85.
- Gault, D.E., Hörz, F., Brownlee, D.E., Hartung, J.B., 1974. Mixing of the lunar regolith. *Geochim. Cosmochim. Acta* 3, 2365–2386.
- Gladstone, G.R., Retherford, K.D., Egan, A.F., Kaufmann, D.E., Miles, P.F., Parker, J.W., Horvath, D., Rojas, P.M., Versteeg, M.H., Davis, M.W., Greathouse, T.K., Slater, D.C., Mukherjee, J., Steffl, A.J., Feldman, P.D., Hurley, D.M., Pryor, W.R., Hendrix, A.R., Mazarico, E., Stern, S.A., 2012. Far-ultraviolet reflectance properties of the Moon's permanently shadowed regions. *J. Geophys. Res. Planet.* 117, E00H04.
- Grieve, R.A.F., Garvin, J.B., 1984. A geometric model for excavation and modification at terrestrial simple impact craters. *J. Geophys. Res. Solid Earth* 89, 11561–11572.
- Hayne, P.O., Hendrix, A., Sefton-Nash, E., Siegler, M.A., Lucey, P.G., Retherford, K.D., Williams, J.-P., Greenhagen, B.T., Paige, D.A., 2015. Evidence for exposed water ice in the Moon's south polar regions from Lunar Reconnaissance Orbiter ultraviolet albedo and temperature measurements. *Icarus* 255, 58–69.
- Head, J.W., 1976. Lunar volcanism in space and time. *Rev. Geophys. Space Phys.* 14, 265–300.
- Huang, Y.-H., Minton, D.A., Hirabayashi, M., Elliott, J.R., Richardson, J.E., Fassett, C.I., Zellner, N.E.B., 2017. Heterogeneous impact transport on the Moon. *J. Geophys. Res.* 122, 1158–1180.
- Hurley, D.M., Lawrence, D.J., Bussey, D.B.J., Vondrak, R.R., Elphic, R.C., Gladstone, G. R., 2012. Two-dimensional distribution of volatiles in the lunar regolith from space weathering simulations. *Geophys. Res. Lett.* 39, L09203.
- Ivanov, B.A., Neukum, G., Wagner, R., 2001. Size-Frequency Distribution of Planetary Impact Craters and Asteroids. In: Marov, M.Y., Rickman, H. (Eds.), *Collisional Processes in the Solar System, Astrophysics and Space Science Library*, vol. 261. Springer, Dordrecht.
- JORC, 2012. Australasian Code for Reporting of Exploration Results, Minerals Resources and Ore Reserves. The Joint Ore Reserves Committee of the Australian Institute of Mining and Metallurgy, Australian Institute of Geoscientists, and Minerals Council of Australia.
- Kloos, J.L., Moores, J.E., Sangha, J., Nguyen, T.G., Schorghofer, N., 2019. The temporal and geographic extent of seasonal cold trapping on the Moon. *J. Geophys. Res. Planets* 124, 1935–1944.
- Kornuta, D., Abbud-Madrid, A., Atkinson, J., Barr, J., Barnhard, G., Bienhoff, D., Blair, B., Clark, V., Cyrus, J., DeWitt, B., Dreyer, C., Finger, B., Goff, J., Ho, K., Kelsey, L., Kervala, J., Kutter, B., Metzger, P., Montgomery, L., Morrison, P., Neal, C., Otto, E., Roesler, G., Schier, J., Seifert, B., Sowers, G., Spudis, P., Sundahl, M., Zacny, K., Zhu, G., 2019. Commercial lunar propellant architecture: a collaborative study of lunar propellant production. *REACH* 13, 100026.
- Lawrence, D.J., 2017. A tale of two poles: toward understanding the presence, distribution, and origin of volatiles at the polar regions of the Moon and Mercury. *J. Geophys. Res. Planets* 122, 21–52.
- Lawrence, D.J., Feldman, W.C., Elphic, R.C., Hagerty, J.J., Maurice, S., McKinney, G.W., Prettyman, T.H., 2006. Improved modeling of Lunar Prospector neutron spectrometer data: implications for hydrogen deposits at the lunar poles. *J. Geophys. Res. Planets* 111, E8.
- Lewis, J.S., 1996. *Mining the Sky: Untold Riches From the Asteroids, Comets, and Planets*. Basic Books, New York, NY (274p).
- Li, S., Lucey, P.G., Milliken, R.E., Hayne, P.O., Fisher, E., Williams, J.-P., Hurley, D.M., Elphic, R.C., 2018. Direct evidence of surface exposed water ice in the lunar polar regions. *PNAS* 115, 8907–8912.
- Lucey, P.G., Costello, E., Hurley, D.M., Prem, P., Farrell, W.M., Petro, N., Cable, M., 2020. Relative Magnitudes of Water Sources to the Lunar Poles. 51st Lunar Planet. Sci. Conf., Abstract #2319.
- Mazarico, E., Neumann, G.A., Smith, D.E., Zuber, M.T., Torrence, M.H., 2011. Illumination conditions of the lunar polar regions using LOLA topography. *Icarus* 22, 1066–1081.
- McGetchin, T.R., Settle, M., Head, J.W., 1973. Radial thickness variation in impact crater ejecta: implications for Lunar Basin deposits. *Earth Planet. Sci. Lett.* 20, 226–236.
- McKay, D.S., Fruland, R.M., Heiken, G.H., 1974. Grain size and the evolution of lunar soils. *Geochim. Cosmochim. Acta* 1, 887–906.
- Melosh, H.J., 1984. Impact ejection, spallation, and the origin of meteorites. *Icarus* 59, 234–260.
- Melosh, H.J., 1989. *Impact Cratering: A Geologic Process*. Oxford University Press, Oxford (253 p).
- Minton, D.A., Fassett, C.I., Hirabayashi, M., Howl, B.A., Richardson, J.E., 2019. The equilibrium size-frequency distribution of small craters reveals the effects of distal ejecta on lunar landscape morphology. *Icarus* 326, 63–87.
- Moores, J.E., 2016. Lunar water migration in the interval between large impacts: heterogeneous delivery to permanently shadowed regions, fractionation, and diffusive barriers. *J. Geophys. Res. Planets* 121, 46–60.
- Morbiddelli, A., Nesvorný, D., Laurenz, V., Marchi, S., Rubie, D.C., Elkins-Tanton, L., Wieczorek, M., Jacobson, S., 2018. The timeline of the lunar bombardment: revisited. *Icarus* 305, 262–276.
- Needham, D.H., Kring, D.A., 2017. Lunar volcanism produced a transient atmosphere around the ancient Moon. *Earth Planet. Sci. Lett.* 478, 175–178.
- Needham, D.H., Siegler, M., Li, S., Kring, D., 2019. Calculated thicknesses of volcanically derived water ice deposits at the lunar poles. In: 50th Lunar Planet. Sci. Conf., Abstract #1087.
- Neish, C.D., Bussey, D.B.J., Spudis, P., Marshall, W., Thomson, B.J., Patterson, G.W., Carter, L.M., 2011. The nature of lunar volatiles as revealed by Mini-RF observations of the LCROSS impact site. *J. Geophys. Res. Planets* 116, E01005.
- Neukum, G., 1983. *Meteoritenbombardement und Datierung Planetarer Oberflächen*. Habilitation Dissertation for Faculty Membership, Univ. of Munich (186 pp).
- Neukum, G., Ivanov, B.A., Hartmann, W.K., 2001. Cratering records in the Inner Solar System in relation to the Lunar Reference System. In: Kallenbach, R., Geiss, J., Hartmann, W.K. (Eds.), *Chronology and Evolution of Mars*, Bern, Switzerland.
- Nozette, S., Spudis, P.D., Robinson, M.S., Bussey, D.B.J., Lichtenberg, C., Bonner, R., 2001. Integration of lunar polar remote-sensing data sets: evidence for ice at the lunar south pole. *J. Geophys. Res. Planets* 106, 23253–23266.
- Ong, L., Asphaug, E.I., Korycansky, D., Coker, R.F., 2010. Volatile retention from cometary impacts on the Moon. *Icarus* 207, 578–589.
- Osinski, G.R., Tornabene, L.L., Grieve, R.A.F., 2011. Impact ejecta emplacement on terrestrial planets. *Earth Planet. Sci. Lett.* 310, 167–181.
- Paige, D.A., Siegler, M.A., Zhang, J.A., Hayne, P.O., Foote, E.J., Bennett, K.A., Vasavada, A.R., Greenhagen, B.T., Schofield, J.T., McCleese, D.J., Foote, M.C., DeJong, E., Bills, B.G., Hartford, W., Murray, B.C., Allen, C.C., Snook, K., Soderblom, L.A., Calcutt, S., Taylor, F.W., Bowles, N.E., Bandfield, J.L., Elphic, R., Ghent, R., Glotch, T.D., Wyatt, M.B., Lucey, P.G., 2010. Diviner lunar radiometer observations of cold traps in the moon's south polar region. *Science* 330, 470–482.
- Pelech, T.M., Roesler, G., Saydam, S., 2019. Technical evaluation of Off-Earth ice mining scenarios through an opportunity cost approach. *Acta Astro* 162, 388–404.
- Pike, R.J., 1974. Craters on Earth, Moon, and Mars: multivariate classification and mode of origin. *Earth Planet. Sci. Lett.* 22, 245–255.
- Pognan, Q., Garraffo, C., Cohen, O., Drake, J.J., 2018. The solar wind environment in time. *ApJ* 856, 53.
- Prem, P., Artemieva, N.A., Goldstein, D.B., Varghese, P.L., Trafton, L.M., 2015. Transport of water in a transient impact-generated lunar atmosphere. *Icarus* 255, 148–158.
- Richardson, J.E., Melosh, H.J., Greenberg, R., 2004. Impact-induced seismic activity on asteroid 433 Eros: a surface modification process. *Science* 306, 1526–1529.
- Robbins, S.J., 2019. *A New Global Database of Lunar Impact Craters >1–2 km: 1. Crater Locations and Sizes, Comparisons With Published Databases, and Global Analysis*. *J. Geophys. Res. Planets* 124, 871–892. https://agupubs.onlinelibrary.wiley.com/doi/abs/10.1029/2018JE005592?casa_token=kh3_QE08H1YAAAAA:soZV4_TiPuh6hG8yOIRtQSVoPhQnK9jAblPqhg2A1CW_rfT4EXlrgEVctUlj1wknPlwSJyMW8sY.
- Rubanenko, L., Aharonson, O., 2017. Stability of ice on the Moon with rough topography. *Icarus* 296, 99–109.
- Rubanenko, L., Venkatraman, J., Paige, D.A., 2019. Thick ice deposits in shallow simple craters on the Moon and Mercury. *Nat. Geosci.* 12, 597–601.
- Runge, I.C., 1998. *Mining Economics and Strategy*. Society for Mining, Metallurgy, and Exploration, Inc, Littleton, CO (316p).
- Schorghofer, N., Aharonson, O., 2014. The lunar thermal ice pump. *ApJ* 788, 169.
- Schultz, P.H., Gault, D.E., 1975. Seismically induced modification of lunar surface features. In: *Proc. Lunar Sci. Conf.* 6th, pp. 2845–2862.
- Siegler, M., Paige, D., Williams, J.-P., Bills, B., 2015. Evolution of lunar polar ice stability. *Icarus* 255, 78–87.
- Siegler, M.A., Miller, R.S., Keane, J.T., Laneville, M., Paige, D.A., Matsuyama, I., Lawrence, D.J., Crotts, A., Poston, M.J., 2016. Lunar true polar wander inferred from polar hydrogen. *Nature* 531, 480–484.
- Sowers, G.F., Dreyer, C.B., 2019. Ice mining in lunar permanently shadowed regions. *New Space* 7, 235–244.
- Space Resource Exploration and Utilization Act of 2015, 2015. H.R. 1508, 114th Cong.
- Spudis, P.D., Bussey, D.B.J., Baloga, S.M., Cahill, J.T.S., Glaze, L.S., Patterson, G.W., Raney, R.K., Thompson, T.W., Thomson, B.J., Ustinov, E.A., 2013. Evidence for water ice on the Moon: results for anomalous polar craters from the LRO Mini-RF imaging radar. *J. Geophys. Res. Planets* 118, 2016–2029.
- Stacy, N.J.S., Campbell, D.B., Ford, P.G., 1997. Arcobio radar mapping of the lunar poles: a search for ice deposits. *Science* 276, 1527–1530.
- Starukhina, L.V., Shkuratov, Y.G., 2000. The lunar poles: water ice or chemically trapped hydrogen? *Icarus* 147, 585–587.

- Stewart, B.D., Pierazzo, E., Goldstein, D.B., Varghese, P.L., Trafton, L.M., 2011. Simulations of a comet impact on the Moon and associated ice deposition in polar cold traps. *Icarus* 215, 1–16.
- Svetsov, V.V., Shuvalov, V.V., 2015. Water delivery to the Moon by asteroidal and cometary impacts. *Planet. Space. Sci.* 117, 444–452.
- Teodoro, L.F.A., Eke, V.R., Elphic, R.C., 2010. Spatial distribution of lunar polar hydrogen deposits after KAGUYA (SELENE). *Geophys. Res. Lett.* 37, L12201.
- Thomson, B.J., Bussey, D.B.J., Neish, C.D., Cahill, J.T.S., Heggy, E., Kirk, R.L., Patterson, G.W., Raney, R.K., Spudis, P.D., Thompson, T.W., Ustinov, E.A., 2012. An upper limit for ice in Shackleton crater as revealed by LRO Mini-RF orbital radar. *Geophys. Res. Lett.* 39, L14201.
- Wang, H.Z., Zhang, J., Shi, Q.Q., Saito, Y., Degeling, A.W., Rae, I.J., Liu, J., Guo, R.L., Yao, Z.H., Tian, A.M., Fu, X.H., Zong, Q.G., Liu, J.Z., Ling, Z.C., Sun, W.J., Bai, S.C., Chen, J., Yao, S.T., Zhang, H., Wei, Y., Liu, W.L., Xia, L.D., Chen, Y., Feng, Y.Y., Fu, S. Y., Pu, Z.Y., 2019. Earth Wind as a Possible Source of Lunar Surface Hydration. arXiv: 1903.04095.
- Watson, K., Murray, B.C., Brown, H., 1961. The behavior of volatiles on the lunar surface. *J. Geophys. Res.* 66, 3033–3045.
- Williams, J.-P., Greenhagen, B.T., Paige, D.A., Schorghofer, N., Sefton-Nash, E., Hayne, P.O., Lucey, P.G., Siegler, M.A., Michael Aye, K., 2019. Seasonal polar temperatures on the Moon. *J. Geophys. Res. Planets* 124, 2505–2521.
- Wilson, L., Head, J.W., Deutsch, A.N., 2019. Volcanically-induced transient atmospheres on the Moon: assessment of duration and significance. In: 50th Lunar Planet. Sci. Conf., Abstract #1343.
- Yang, F., Xu, Y., Chan, K.L., Zhang, X., Hu, G., Li, Y., 2019. Study of Chang'E-2 microwave radiometer data in the lunar polar region. *Adv. Astro.* 2019, 3940837.
- Zeller, E.J., Ronca, L.B., Levy, P.W., 1966. Proton-induced hydroxyl formation on the lunar surface. *J. Geophys. Res.* 71, 4855–4860.
- Zhang, J.A., Paige, D.A., 2010. Correction to “cold-trapped organic compounds at the poles of the Moon and Mercury: implications for origins”. *Geophys. Res. Lett.* 27, L03203.
- Zhu, C., Gillis-Davis, J.J., Crandall, P.B., Ishii, H.A., Bradley, J.P., Corley, L.M., Kaiser, R. I., 2019. Untangling the formation and liberation of water in the lunar regolith. *Proc. Natl. Acad. Sci.* 116 (23), 11165–11170. <https://doi.org/10.1073/pnas.1819600116>.
- Zimmerman, M.I., Farrell, W.M., Stubbs, T.J., 2013. Recursive plasma wake formation on the Moon and its effect on polar volatiles. *Icarus* 226, 992–998.